

# Numbers of presynaptic $\text{Ca}^{2+}$ channel clusters match those of functionally defined vesicular docking sites in single central synapses

Takafumi Miki<sup>a,1</sup>, Walter A. Kaufmann<sup>b</sup>, Gerardo Malagon<sup>a</sup>, Laura Gomez<sup>a</sup>, Katsuhiko Tabuchi<sup>c,d</sup>, Masahiko Watanabe<sup>e</sup>, Ryuichi Shigemoto<sup>b,1,2</sup>, and Alain Marty<sup>a,1,2</sup>

<sup>a</sup>Laboratoire de Physiologie Cérébrale, CNRS UMR 8118, Université Paris Descartes, 75006 Paris, France; <sup>b</sup>Institute of Science and Technology Austria, A-3400 Klosterneuburg, Austria; <sup>c</sup>Department of Molecular and Cellular Physiology, Shinshu University School of Medicine, Matsumoto 390-8621, Japan; <sup>d</sup>Institute for Biomedical Sciences, Interdisciplinary Cluster for Cutting Edge Research, Shinshu University, Matsumoto 390-8621, Japan; and <sup>e</sup>Department of Anatomy, Graduate School of Medicine, Hokkaido University, Sapporo 060-8638, Japan

Edited by Reinhard Jahn, Max Planck Institute for Biophysical Chemistry, Goettingen, Germany, and approved May 16, 2017 (received for review March 17, 2017)

Many central synapses contain a single presynaptic active zone and a single postsynaptic density. Vesicular release statistics at such “simple synapses” indicate that they contain a small complement of docking sites where vesicles repetitively dock and fuse. In this work, we investigate functional and morphological aspects of docking sites at simple synapses made between cerebellar parallel fibers and molecular layer interneurons. Using immunogold labeling of SDS-treated freeze-fracture replicas, we find that  $\text{Ca}_v2.1$  channels form several clusters per active zone with about nine channels per cluster. The mean value and range of intersynaptic variation are similar for  $\text{Ca}_v2.1$  cluster numbers and for functional estimates of docking-site numbers obtained from the maximum numbers of released vesicles per action potential. Both numbers grow in relation with synaptic size and decrease by a similar extent with age between 2 wk and 4 wk postnatal. Thus, the mean docking-site numbers were 3.15 at 2 wk (range: 1–10) and 2.03 at 4 wk (range: 1–4), whereas the mean numbers of  $\text{Ca}_v2.1$  clusters were 2.84 at 2 wk (range: 1–8) and 2.37 at 4 wk (range: 1–5). These changes were accompanied by decreases of miniature current amplitude (from 93 pA to 56 pA), active-zone surface area (from  $0.0427 \mu\text{m}^2$  to  $0.0234 \mu\text{m}^2$ ), and initial success rate (from 0.609 to 0.353), indicating a tightening of synaptic transmission with development. Altogether, these results suggest a close correspondence between the number of functionally defined vesicular docking sites and that of clusters of voltage-gated calcium channels.

neurotransmitter release | active zone | calcium channel | release site | parallel fiber

In presynaptic terminals, the active zone (AZ) represents a highly specialized structure allowing the binding and  $\text{Ca}^{2+}$ -dependent release of synaptic vesicles (SVs) (1). Fluctuation analysis of synaptic signals suggests the presence of one or several functional units per AZ (2, 3). These units are either called “release sites” or “docking sites,” and their number per AZ represents the maximum SV output that this structure can provide per action potential (AP). In recent years, optical methods have been developed to record single-SV release (4). Notably, studies using superresolution and total internal reflection fluorescence imaging in functioning central synapses have provided information on the kinetics (5) and sub-synaptic localization (6) of single-SV docking and release. Despite these advances, electrophysiological methods remain the most rapid and sensitive method to assess SV exocytosis at central synapses such as the calyx of Held (7) or cerebellar mossy fiber terminals (8). In recent years, electrophysiological recordings performed at special synapses containing a single AZ and a single postsynaptic density (PSD), called “simple synapses,” revealed a fixed maximum in the number of SVs that can be released per AZ by a short calcium stimulus (9–11), providing a direct evaluation of the number of docking sites per AZ. This number ranges between

1 and 6 at synapses between molecular layer interneurons (MLIs) of the cerebellum and between 3 and 6 at synapses between parallel fibers (PFs) and MLIs (9–11). However, even in these special cases, we still do not know precisely what the morphological counterpart of a functionally defined docking site is.

In molecular terms, docking sites are thought to be composed of a multiprotein assembly including RIM, RIM-binding protein, Munc13, Munc18, and SNARE proteins (1, 6, 12). This protein complex interacts with presynaptic voltage-gated  $\text{Ca}^{2+}$  channels (VGCCs) (1). Furthermore, the remarkably short duration of synaptic delay (13), as well as analysis of the inhibition of synaptic release by VGCC blockers or by slow-binding  $\text{Ca}^{2+}$  buffers in certain synapses (reviews: refs. 14–16), put constraints on the distance separating SV-binding sites from VGCCs. Therefore, a promising path to studying docking sites is to examine VGCC distribution within the AZ.

In certain synapses, electron microscopy and/or superresolution optical imaging have delivered a precise picture of the interaction between VGCCs and SVs. In vertebrate neuromuscular junctions, AZs appear as elongated structures where SVs dock (17). In freeze-fracture replicas, SV fusion sites flank double rows of proteins presumably representing VGCCs (18). In frog neuromuscular

## Significance

Release–docking sites have been considered from a morphological point of view as the sites where synaptic vesicles dock and fuse with the active-zone membrane. Functionally, docking sites limit the maximum number of vesicles released per action potential, determining synaptic strength. Until now it has not been possible to establish a clear link between morphological and functional aspects of docking sites in mammalian brain synapses. Recent data suggest that calcium channels form several clusters in the active zone. Here, we show that the number of the clusters matches that of functional docking sites and both parameters change in parallel with age and synaptic size. Based on these results we propose a one-to-one correspondence between docking sites and calcium channel clusters.

Author contributions: T.M., R.S., and A.M. designed research; T.M., W.A.K., G.M., and L.G. performed research; K.T. and M.W. contributed new reagents/analytic tools; T.M. and A.M. analyzed data; and T.M., R.S., and A.M. wrote the paper.

The authors declare no conflict of interest.

This article is a PNAS Direct Submission.

Freely available online through the PNAS open access option.

<sup>1</sup>To whom correspondence may be addressed. Email: takafumi.miki@parisdescartes.fr, ryuichi.shigemoto@ist.ac.at, or alain.marty@parisdescartes.fr.

<sup>2</sup>R.S. and A.M. contributed equally to this work.

This article contains supporting information online at [www.pnas.org/lookup/suppl/doi:10.1073/pnas.1704470114/-DCSupplemental](http://www.pnas.org/lookup/suppl/doi:10.1073/pnas.1704470114/-DCSupplemental).

junctions, SVs dock externally to the presumed VGCCs, forming two parallel and external rows of docking sites (19, 20) whereas in the mouse they dock between the two rows of VGCCs, forming a single central line of docking sites (21); in each case, specific cytoskeletal elements link SVs, VGCCs, and plasma membrane together. Interestingly, in the mouse neuromuscular junction, estimates for the number of docking sites located inside the two rows of VGCCs and for the size of the readily releasable pool of SVs coincide at two per active zone (22). In the fly neuromuscular junction, superresolution optical imaging studies indicate a circular organization with a cluster of VGCCs in the center, several SVs docked next to the VGCCs, and additional SVs linked to VGCCs by bruchpilot proteins, presumably waiting for docking (23, 24). However, precise release statistics are difficult to obtain in giant synapses such as neuromuscular junction preparations, making estimates of functional docking-site numbers uncertain.

In mammalian central synapses, information concerning the spatial arrangement of SVs and VGCCs remains scarce and fragmentary. Electron microscopy studies indicate the presence of several docked SVs per AZ with average numbers of approximately eight at PF or climbing fiber terminals (25) and two to seven at the calyx of Held (26–28). Such numbers, however, are merely indicative of docking-site numbers because SVs may bind to the plasma membrane without being fully release-competent (5) whereas, conversely, only 50–70% of docking sites are occupied by SVs at rest (10, 11, 29).

Using selective  $\text{Ca}_v2.1$  antibodies on SDS-treated freeze-fracture replicas, clusters of presynaptic VGCCs were identified in individual AZs of central mammalian synapses (hippocampal synapses: refs. 30, 31; PF–Purkinje cell (PC) synapses: refs. 32, 33; and calyx of Held: ref. 34). These studies raise the possibility of a link between docking sites and VGCC clusters. More specifically, we hypothesize in the present work that, in these preparations, each a VGCC

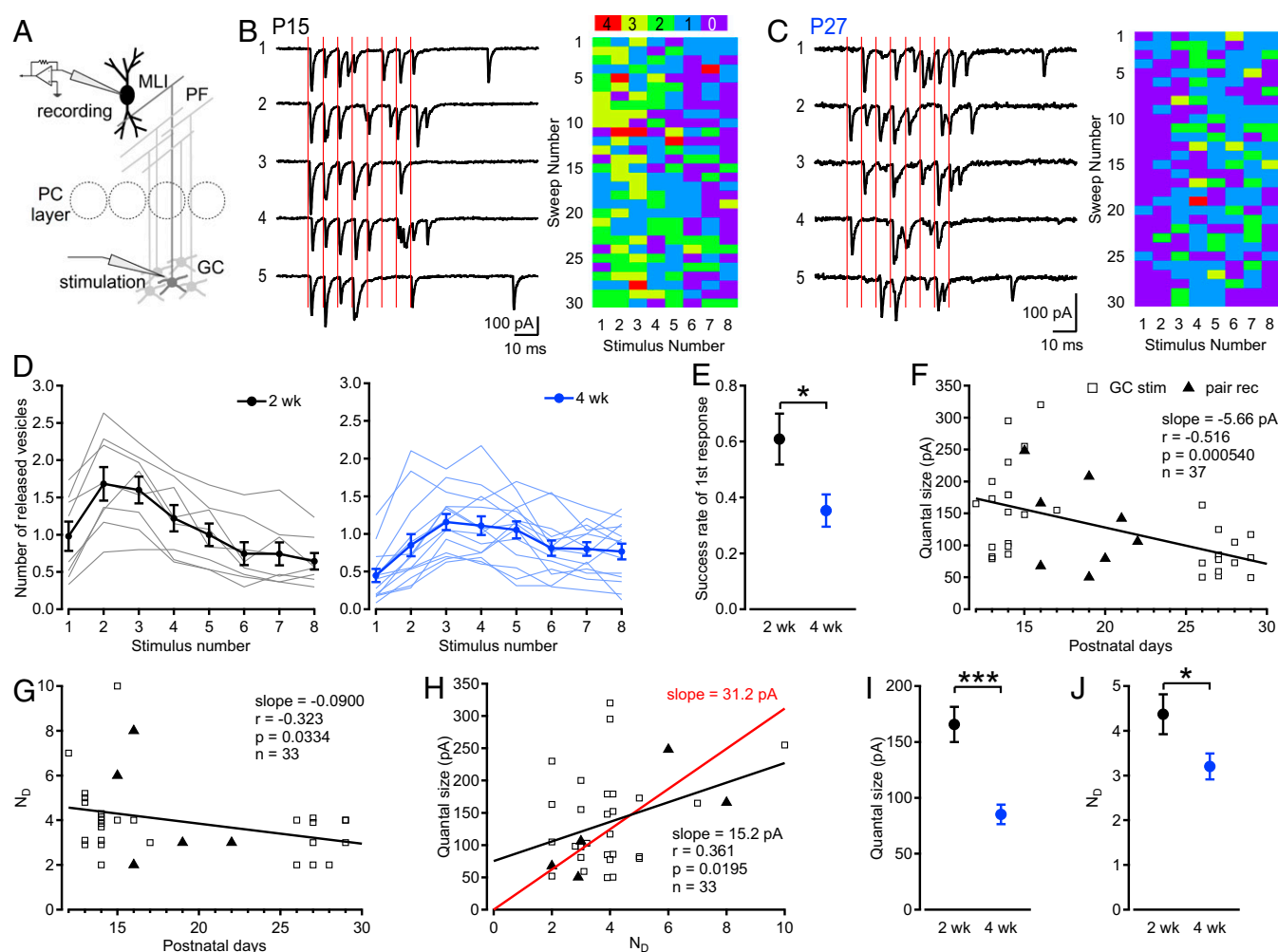


**Fig. 1.** Developmental changes of pre- and postsynaptic functional parameters at simple PF–MLI synapses. (A) Schematic of recording conditions. In a parasagittal slice, synaptic responses are recorded in an MLI. A monopolar stimulation pipette is positioned near a GC; the corresponding PF contacts the MLI at a single bouton. PC, Purkinje cell. (B and C) EPSCs elicited by trains of extracellular stimulation (red lines: timing of stimulation at 200 Hz; intertrain intervals: 10 s) at 2 wk and 4 wk. Tables show color-coded numbers of released SV as a function of stimulus number and sweep number. (D) Released SV number as a function of stimulus number at 2 wk (black,  $n = 8$ ; thin lines, individual experiments; thick lines, averages  $\pm$  SEM) and 4 wk (blue,  $n = 14$ ). (E) Success rate of first response at 2 wk ( $0.609 \pm 0.091$ ,  $n = 8$ ) and 4 wk ( $0.353 \pm 0.058$ ,  $n = 14$ ). (F) Quantal amplitude decreases as a function of age (black regression line;  $P = 0.0005$ ). GCs were stimulated either by an extracellular monopolar pipette (open squares) or by a cell-attached pipette (paired recordings, filled triangles). (G) Likewise, a plot of  $N_D$  as a function of postnatal day shows a significant downward trend (black regression line;  $P = 0.03$ ). (H) Quantal amplitude and  $N_D$  are significantly correlated, indicating that the two parameters covary with synaptic size (black regression line;  $P = 0.02$ ). A regression line constrained to pass through the origin has a slope of 31.2 pA (red). (I) Quantal size is larger at 2 wk than at 4 wk. (J)  $N_D$  is likewise larger at 2 wk than at 4 wk (one-tailed  $t$  test). Error bars show  $\pm$  SEM. \* $P < 0.05$  and \*\*\* $P < 0.001$ , Student's  $t$  test.

cluster represents a single docking site. This scheme predicts that the number of functional docking sites and that of VGCC clusters should be identical. In the following, we estimate these two numbers at simple PF–MLI synapses, asking the following questions: (i) Are mean values similar for the two numbers? (ii) Are inter-synaptic variations similar for the two numbers, and, if yes, what determines these variations? (iii) Are changes during development parallel for the two numbers?

## Results

**Developmental Changes at Simple PF–MLI Synapses.** In the present work, we examine how simple synapse properties evolve as a function of age. For this purpose, we compare simple PF–MLI synapses at postnatal day 13 (P13)–P16 and P26–P29 (respectively called “2-wk data” and “4-wk data” hereafter). At 4 wk, however, the growing density of PF–MLI innervation jeopardized the method of stimulation of individual PFs used previously to obtain simple synapse recordings (9). Therefore, instead of using extracellular stimulation in the molecular layer, we used in the present work either local extracellular stimulation in the granule cell (GC) layer or paired GC–MLI recordings (Fig. 1*A*) (35). As in previous studies (9, 29), we obtained uniform event amplitudes in response to train stimulation, indicating that a single synaptic connection was stimulated. Using a mean quantal excitatory postsynaptic current (EPSC) trace obtained from delayed asynchronous responses as a template, we deconvolved multiquantal EPSCs to estimate the number of SVs released by each stimulus (Fig. 1*B* and *C*). We fixed the extracellular  $\text{Ca}^{2+}$  concentration to 3 mM to optimize SV counting (9). Plots of mean released SV number as a function of stimulus number revealed a facilitation-depression sequence at both 2 wk and 4 wk (Fig. 1*D*). At 2 wk, the response peaked at the second stimulation as previously reported (29), whereas the 4-wk data displayed a lower initial mean value and a slower facilitation peaking at the third stimulation before converging with 2-wk data at the end of the train. The success rate of the first response was lower at 4 wk than at 2 wk (Fig. 1*E*), suggesting a lower release probability at 4 wk.

To explore possible developmental changes of postsynaptic properties, we next plotted quantal size values derived from simple synapse recordings as a function of age. This plot revealed a significant downward trend (Fig. 1*F*). In view of previous evidence linking quantal size, number of postsynaptic receptors, and postsynaptic density (PSD) size (36–38), these results suggest a decrease of the PSD size with age.

Next, we fitted distributions of released SV numbers using a binomial model (Fig. S1) (9), and we derived from these fits functional estimates of the number of docking sites,  $N_D$ . To improve the accuracy of  $N_D$  estimates,  $N_D$  was determined for the stimulus number corresponding to maximal release probability at the peak of synaptic facilitation (9). Plotting  $N_D$  as a function of age revealed a significant decrease (Fig. 1*G*). In simple GABAergic synapses, variations in quantal size are related with variations in  $N_D$ , and both parameters are thought to scale with synaptic size (10, 11). To test whether size variations could underlie the parallel downward trends observed for quantal size and  $N_D$ , we plotted the quantal size as a function of  $N_D$ , revealing a significant correlation between these two parameters (Fig. 1*H*; unrestrained regression line in black; regression line through the origin in red). These results suggest that a reduction of synaptic size could act as a common factor underlying changes in quantal size and in  $N_D$  during development.

In conclusion, simple synapse recordings reveal a parallel decrease of quantal size and  $N_D$  with age, as illustrated in Fig. 1*I* and *J* for 2-wk and 4-wk group data. Quantal size values were  $166 \text{ pA} \pm 16 \text{ pA}$  at 2 wk (mean  $\pm$  SEM;  $n = 21$ ) and  $85 \text{ pA} \pm 9 \text{ pA}$  at 4 wk (mean  $\pm$  SEM;  $n = 14$ ).  $N_D$  values were  $4.37 \pm 0.45$  at 2 wk (mean  $\pm$  SEM;  $n = 19$ ) and  $3.20 \pm 0.29$  at 4 wk (mean  $\pm$  SEM;  $n = 10$ ). The initial release probability per

docking site (obtained in response to the first AP in a train) was  $0.29 \pm 0.05$  at 2 wk and  $0.14 \pm 0.03$  at 4 wk; corresponding maximum release probability values per docking site (obtained at the peak of facilitation, usually after the second AP at 2 wk and after the third AP at 4 wk) were  $0.53 \pm 0.03$  at 2 wk and  $0.41 \pm 0.04$  at 4 wk.

**Correcting Mean Docking-Site Number for Recording Bias.** Before accepting the above  $N_D$  values for further quantification, we asked whether these values could be biased due to our experimental procedures. Specifically, it seemed possible that large-size synapses with large quantal sizes and large  $N_D$  values were overrepresented in our recordings. To find simple synapses, we locally apply an elevated  $\text{K}^+$  solution, and we search for  $\text{K}^+$ -evoked bursts of EPSCs with homogeneous amplitudes. Synapses with high quantal size provide more prominent, more easily identifiable bursts and are therefore more likely to be selected. Any bias to select high quantal sizes would be reflected by high  $N_D$  values because the two parameters are correlated, as shown in Fig. 1*H*. To test this possibility, we compared the distribution of quantal sizes obtained in simple synapses with the distribution of quantal sizes obtained from miniature EPSCs (mEPSCs) (Fig. 2). The distribution of quantal sizes in simple synapse recordings should reflect that of mEPSCs if there were no bias. We found that quantal sizes of evoked EPSCs (“qEPSCs”) and mEPSC amplitudes spanned similar ranges both at 2 wk (Fig. 2*A* and *D*) and at 4 wk (Fig. 2*B* and *E*) and that amplitude distributions for both types of signals shifted significantly to smaller values with age (Fig. 2*C* and *F*). However, small amplitudes were more prominent in mEPSC distributions, leading to lower mean values ( $93.2 \text{ pA}$  at 2 wk and  $55.6 \text{ pA}$  at 4 wk) and higher skews ( $1.97$  at 2 wk and  $1.33$  at 4 wk) compared with distributions of qEPSCs (mean:  $129.0 \text{ pA}$  at 2 wk and  $87.3 \text{ pA}$  at 4 wk; skew:  $1.10$  at 2 wk and  $1.02$  at 4 wk). This result indicated that our analysis had a recording bias and that synapses with a large quantal size were overrepresented in our simple synapse recordings. To correct for this bias, we assumed in agreement with previous

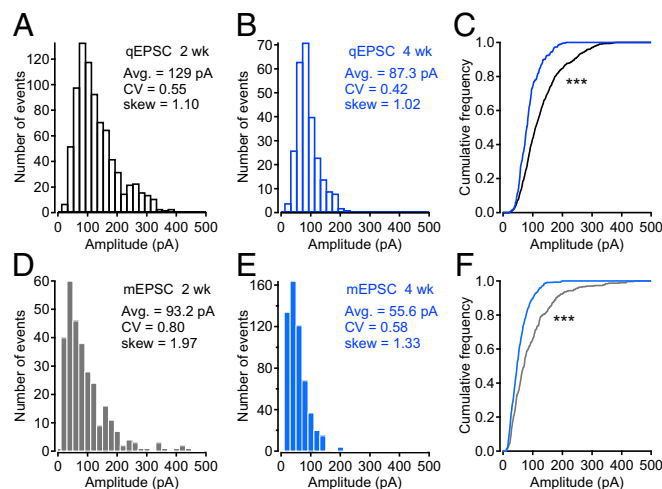


**Fig. 2.** Amplitude distributions of evoked quantal EPSCs and of miniature EPSCs in MLIs. (*A* and *B*) Amplitude distribution of first single events evoked by GC stimulation in simple synapse recordings at 2 wk (from 19 cells, *A*) and 4 wk (from 10 cells, *B*). First events were selected for this analysis to avoid desensitization and amplitude occlusion following multiple EPSCs, as previously explained (9). (*C*) Cumulative frequency plots for evoked quantal EPSC amplitudes at 2 wk (black) and 4 wk (blue). (*D* and *E*) Amplitude distribution of mEPSC obtained in the presence of tetrodotoxin at 2 wk (from nine cells, *D*) and 4 wk (from six cells, *E*). (*F*) Cumulative frequency plots for mEPSC amplitude at 2 wk (black) and 4 wk (blue). \*\*\* $P < 0.001$ , Kolmogorov–Smirnov test.



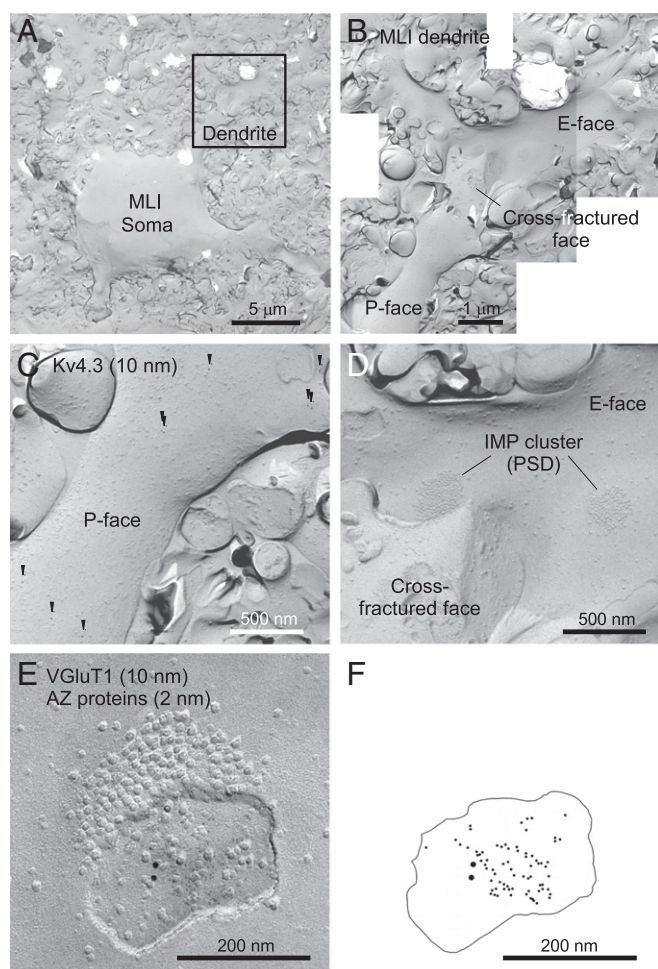


**Fig. 3.** Identification of PF-MLI synapses. (A) An MLI profile in the cerebellar molecular layer in a replica from a P15 rat. (B) Blow-up of squared region in A. A P-face, a cross-fractured face, and an E-face are apparent next to each other in the MLI dendrite. (C) Immunogold particles for Kv4.3 (10 nm) are found in the P-face (arrowheads), confirming identification of the structure as belonging to an MLI. (D) IMP clusters with high density are found in the E-face. (E) An AZ in a PF bouton displays its P-face including labeling for VGLUT1 (10 nm) and for the AZ proteins RIM, ELKS, and neurexin (2 nm). A transition occurs from the presynaptic P-face to the postsynaptic E-face in this terminal, revealing the dense IMP aggregate characteristic of PF-MLI synapses. (F) Positions of gold particles for VGLUT1 (large dots) and AZ proteins (small dots) in E. The border between postsynaptic E-face and presynaptic P-face is delineated.

studies (10, 11, 31, 38) that both quantal size and  $N_D$  are proportional to synaptic size, so that the ratio between the two parameters is constant across synapses at each of the two ages. Accordingly, we calculated the ratio of average values between miniature and quantal-evoked events and multiplied  $N_D$  values by this ratio (ratio: 0.72 for 2 wk and 0.64 for 4 wk). Corrected  $N_D$  values are 3.15 at 2 wk and 2.03 at 4 wk. Comparison of amplitude distributions for mEPSCs and qEPSCs suggested that missed synapses often had one to two docking sites. After correction, the range of  $N_D$  is 1–10 at 2 wk and 1–4 at 4 wk, respectively.

**Parameters of Two-Step Model at 2 Wk and 4 Wk.** We recently proposed that if a docking site becomes empty, reoccupancy depends on the supply of a new SV provided by an associated replacement site (two-step model) (29). Key evidence for the two-step model came from an examination of variance-mean plots of cumulative numbers of vesicular release events. Comparing such plots at 2 wk and 4 wk revealed a steeper increase of the cumulative variance

with mean at 4 wk than at 2 wk (Fig. S2). Monte Carlo simulations of these results indicated that, at 4 wk, the release probability of docked SVs is reduced for the first and second stimulation, possibly reflecting a decrease of the percentage of high release probability “superprimed” SVs (39, 40). In addition, simulations indicated a reduction of the initial occupancy of the replacement site at 4 wk (Fig. S2).

**Identification of PF-MLI Synapses in SDS-Digested Freeze-Fracture Replica Labeling.** To investigate the 2D distribution of VGCCs in an AZ with nanoscale resolution, we performed SDS-digested freeze-fracture replica labeling (SDS-FRL) for  $Ca_v2.1$  because this VGCC subtype predominates in PF terminals (41). This study was performed on sagittally cut cerebellar slices to match the conditions of electrophysiology experiments.

For quantitative comparisons of morphological and physiological data, it is essential to restrict morphological results to the appropriate category of synapses. Therefore, we next aimed at identifying PF-MLI synapses in a replica sample. MLI somata and dendrites could be unambiguously identified in a replica obtained from the molecular layer of the cerebellum as previously reported (Fig. 3 A and B) (37). MLI dendrites are free of spines, unlike PC dendrites. Immunogold particles for Kv4.3, a specific marker for MLI (42), were observed on the protoplasmic face (P-face), confirming MLI identification (Fig. 3C). We sometimes found straight, unbranched, Kv4.3-negative aspiny dendrites in the molecular layer. These profiles likely originate from Golgi cells. On the MLI exoplasmic face (E-face), we observed groups of densely packed intramembrane particles (IMP) representing PSDs of excitatory synapses (Fig. 3D) (37). On MLI dendrites, profiles occasionally displayed a transition between presynaptic P-face and postsynaptic E-face with an associated IMP cluster within the same synapse. These profiles showed double labeling by AZ proteins and VGLUT1 (Fig. 3 E and F). Because VGLUT1 is selectively expressed in PF boutons in the molecular layer (43), these results confirm that these profiles originate from PF-MLI synapses. We also found that the presynaptic P-face of these synapses was flat, in contrast to the concave profile observed at PF-PC synapses (33); this difference provides an additional criterion to distinguish between PF-MLI and PF-PC synapses. Finally, we

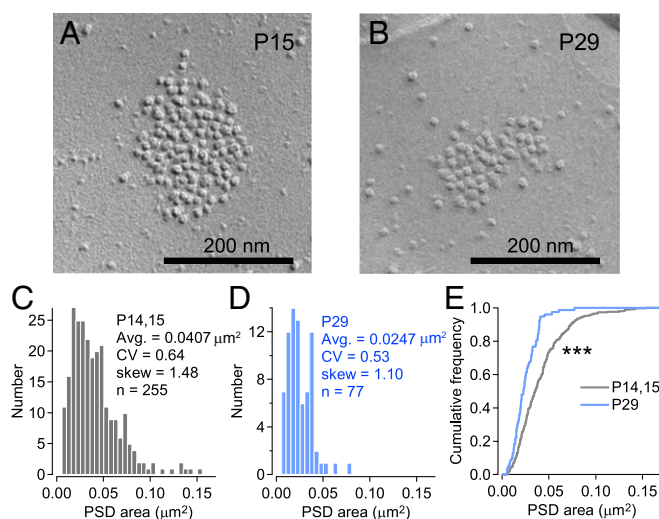


**Fig. 4.** Developmental changes of E-face IMP clusters in MLI dendrites. (A and B) Representative E-face IMP clusters at 2 wk (A) and 4 wk (B). (C and D) Distribution histograms for IMP cluster area at 2 wk (C; mean  $\pm$  SD =  $0.0407 \mu\text{m}^2 \pm 0.0262 \mu\text{m}^2$ ), and 4 wk (D; mean  $\pm$  SD =  $0.0247 \mu\text{m}^2 \pm 0.0131 \mu\text{m}^2$ ). (E) Corresponding cumulative plots for IMP cluster sizes at 2 wk (gray line) and 4 wk (blue line). \*\*\* $P < 0.001$ , Kolmogorov-Smirnov test.

occasionally found GABAergic synapses on MLIs by double labeling for AZ proteins and VGAT (Fig. S3). However, experiments using triple labeling for VGluT1, VGAT, and AZ proteins revealed that the proportion of glutamatergic synapses in afferent MLI synapses was 97.9% (93/95), the rest (2.1%, 2/95) being GABAergic (i.e., MLI–MLI synapses). This result indicates a very small proportion of inhibitory synapses. Overall, we could identify presynaptic AZ regions of PF–MLI synapses by combining AZ protein labeling and morphological identification of MLIs in a replica, even though a small contamination of GABAergic synapses would be included in the synapses observed without VGluT1 and VGAT labeling.

**Morphological Changes of PF–MLI Synapse with Age.** We next examined developmental changes of the PSD area. PSD areas of excitatory synapses are associated with IMP aggregates that contain AMPA receptors (37) and that appear on the E-face of MLI dendrites (44, 45). Therefore, we measured the IMP cluster area to estimate the PSD area (Fig. 4*A* and *B*). We found that the PSD area decreased from 2 wk (mean  $\pm$  SD =  $0.0407 \mu\text{m}^2 \pm 0.0262 \mu\text{m}^2$ ; Fig. 4*C*) to 4 wk (mean  $\pm$  SD =  $0.0247 \mu\text{m}^2 \pm 0.0131 \mu\text{m}^2$ ; Fig. 4*D*), a significant change (Fig. 4*E*).

To examine presynaptic changes with age, we measured the AZ area at 2 wk and 4 wk. In PF–MLI synapses, we could not find any distinctive structural feature to recognize the AZ region on the P-face of the presynaptic membrane. Therefore, to locate the AZ, we labeled simultaneously three well-known AZ markers: RIM, ELKS, and neuroligin. Using 2-nm and 5-nm gold particles, respectively, for this mix of AZ proteins and for the  $\text{Ca}_v2.1$  subunit (Fig. 5*A–F*), we gathered PF–MLI synapse images in which (i) an entire AZ region displayed its presynaptic P-face; (ii) this presynaptic P-face exhibited both 2-nm and 5-nm particles (Fig. 5*C–F*). To measure the AZ area, we delineated a convex polygon using the outermost particles (2/5 nm) contained in one AZ (Fig. 5*D* and *F* and Fig. S4). We analyzed AZ area sizes at 2 wk and 4 wk by measuring the area of this polygon (Fig. S4). In accord with previous results (e.g., 46), AZ size distributions were indistinguishable from those of PSD area at both 2 wk and 4 wk (Fig. S4). Confirming the above results on PSD area distribution (Fig. 4*E*), we found that AZ area is larger at 2 wk (mean  $\pm$  SD =  $0.0427 \mu\text{m}^2 \pm 0.0242 \mu\text{m}^2$ ; Fig. 5*G*) than at 4 wk (mean  $\pm$  SD =  $0.0234 \mu\text{m}^2 \pm 0.0135 \mu\text{m}^2$ ; Fig. 5*H* and *I*).

In conclusion, the size of PF–MLI synapses sharply decreases with age. Assuming that receptor density remains constant, as

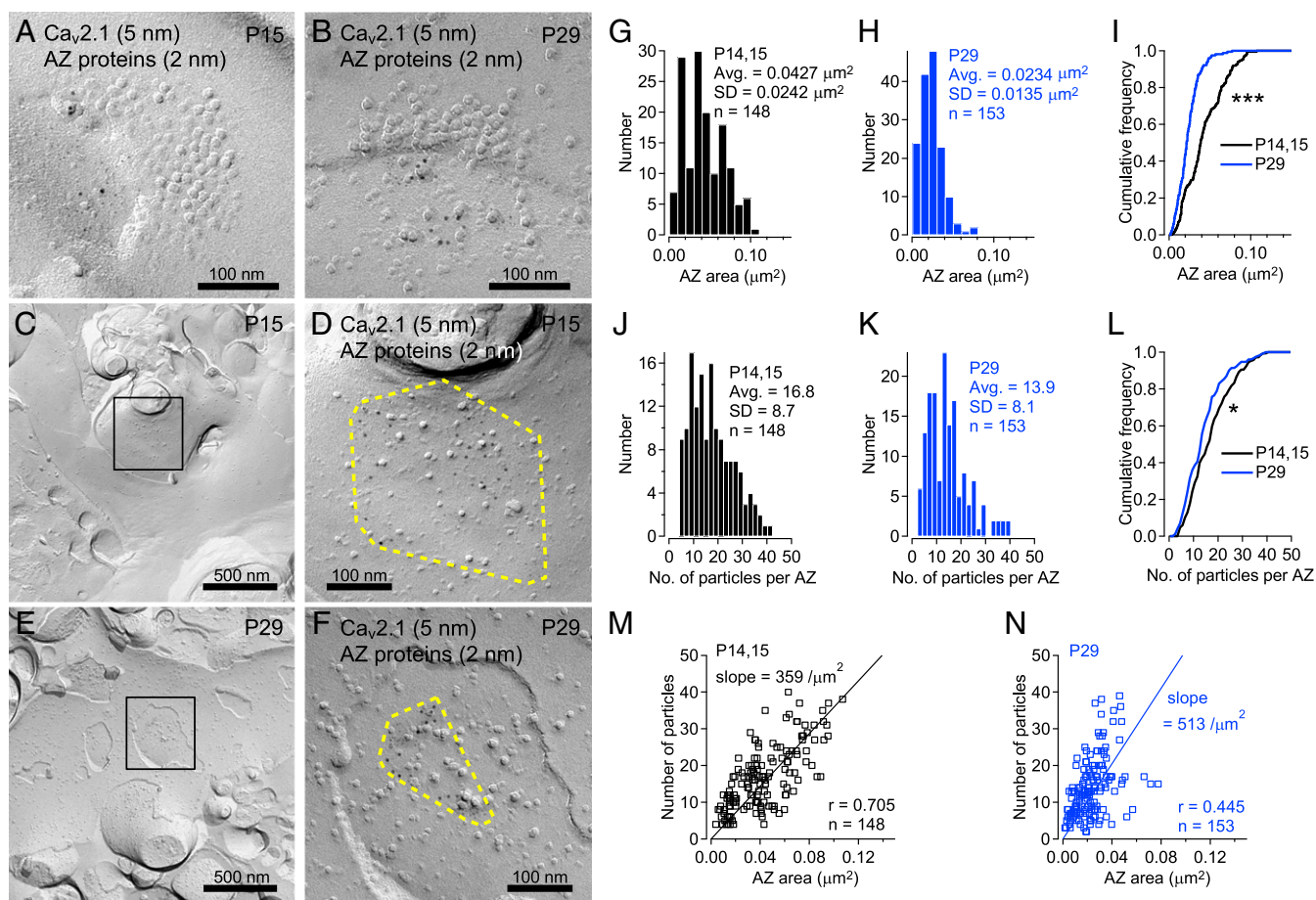


**Fig. 5.** Presynaptic  $\text{Ca}_v2.1$  channel labeling in AZs. (A and B) Representative  $\text{Ca}_v2.1$  labeling in partial AZs associated with complementary partial PSDs represented by postsynaptic E-face IMP clusters in MLI dendrites at 2 wk (A) and 4 wk (B). (C–F) Representative  $\text{Ca}_v2.1$  labeling in full AZ areas connecting with MLI dendrites at 2 wk (C and D) and 4 wk (E and F). (D and F) Blow-up images of C (D) and of E (F) show  $\text{Ca}_v2.1$  and AZ proteins labeling (5 nm and 2 nm, respectively) inside area limited by yellow dashed lines. Detailed methods to measure AZ area are shown in Fig. S4. (G and H) Distribution histograms of AZ area at 2 wk (G: mean  $\pm$  SD =  $0.0427 \mu\text{m}^2 \pm 0.0242 \mu\text{m}^2$ ) and 4 wk (H: mean  $\pm$  SD =  $0.0234 \mu\text{m}^2 \pm 0.0135 \mu\text{m}^2$ ). (I) Cumulative frequency plots for AZ area at 2 wk (black line) and 4 wk (blue line). (J and K) Distribution histograms of the number of gold particles for  $\text{Ca}_v2.1$  labeling per AZ at 2 wk (J: mean  $\pm$  SD =  $16.8 \pm 8.7$ ) and 4 wk (K: mean  $\pm$  SD =  $13.9 \pm 8.1$ ). (L) Cumulative frequency plots for the number of gold particles labeling  $\text{Ca}_v2.1$  within presynaptic AZs. (M and N) Correlation between the number of gold particles labeling  $\text{Ca}_v2.1$  and the AZ area at 2 wk (M:  $n = 148$  AZs) and 4 wk (N:  $n = 153$  AZs). \* $P < 0.05$  and \*\*\* $P < 0.001$ , Kolmogorov–Smirnov test.



suggested by the finding of very high and homogenous AMPA receptor density at PF–MLI synapses (37) and the finding of the close packing arrangement of IMPs both at 2 wk and 4 wk, these results indicate that AMPA receptor numbers decrease with age, in agreement with the smaller quantal size found at 4 wk compared with 2 wk (Figs. 1I and 2F). On the presynaptic side, the decrease of AZ size is consistent with the decrease in  $N_D$  obtained from functional measurements (Fig. 1J).

**Analysis of VGCC Distribution.** To identify morphological counterparts of docking sites, we next analyzed the VGCC labeling in individual AZs. The number of  $\text{Ca}_v2.1$  labeling per AZ decreased slightly but significantly with age (mean  $\pm$  SD:  $16.8 \pm 8.7$  at 2 wk, and  $13.9 \pm 8.1$  at 4 wk; Fig. 5J–L). Using a previously reported method (33), we estimated  $\text{Ca}_v2.1$ -labeling efficiency in our replicas at 62% (see details in *SI Materials and Methods*). Correcting the above  $\text{Ca}_v2.1$ -labeling numbers with this percentage yielded total mean VGCC numbers per AZ of 27 at 2 wk and 22 at 4 wk. We further found that the number of  $\text{Ca}_v2.1$  labelings per AZ was correlated with the size of the AZ area at 2 wk and 4 wk as previously reported in hippocampal glutamatergic synapses (Fig. 5M and N) (31). From the slope of the linear fit, we obtained density values of  $\text{Ca}_v2.1$  labeling of  $359 \pm 23$  and  $513 \pm 49$  gold particles/ $\mu\text{m}^2$  (mean  $\pm$  95% CI;  $t$  test on slopes:  $P < 0.001$ ; estimated VGCC density of 579 and 827/ $\mu\text{m}^2$ ) in AZs of 2 wk and 4 wk, respectively. Therefore, the density of  $\text{Ca}_v2.1$  channels increases during development.

Next, we looked into the distribution of  $\text{Ca}_v2.1$  channels in each AZ. In accord with previous reports (30, 31, 33), we found that  $\text{Ca}_v2.1$  channel labels were not distributed uniformly. The distribution of distances between any pair of particles within an AZ displayed a peak in the range between 0 nm and 50 nm (particularly evident in 4-wk data), indicating particle association within clusters, whereas beyond this range particle distances were distributed broadly (Fig. 6A and B). We performed Monte Carlo simulations assuming random distributions of the observed number of 5-nm particles in individual AZ areas determined from the 2/5-nm particles, as well as an exclusion zone of 5 nm around each particle to account for steric hindrance. As may be seen in Fig. 6A and B (red curves), these random distribution models do not display the biphasic distributions

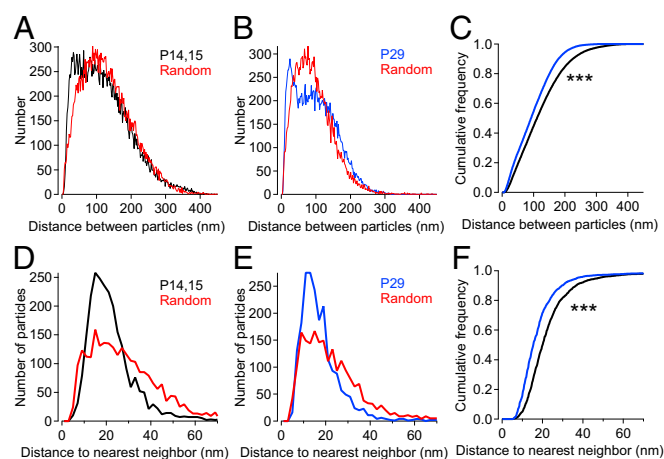


**Fig. 6.**  $\text{Ca}_v2.1$  channel clustering within the AZ. (A and B) Distributions of interparticle distances within each AZ at 2 wk (A) and 4 wk (B). (C) Cumulative distributions of interparticle distances at 2 wk (black) and 4 wk (blue). (D and E) Distributions of nearest neighbor distances of gold particles labeling  $\text{Ca}_v2.1$  within each AZ. Monte Carlo simulations for random distributions with uniform particle density and an exclusion zone of 5 nm around each particle could not reproduce experimental distributions (red lines in A and B and D and E). (F) Cumulative distributions of nearest neighbor distances. \*\*\* $P < 0.001$ , Kolmogorov–Smirnov test.

observed experimentally and markedly differ from data in the 10- to 150-nm range (Kolmogorov–Smirnov test on cumulated distributions:  $P < 0.001$  at 2 wk and  $P < 0.001$  at 4 wk). Furthermore, the distributions of nearest neighbor distances between particles were significantly different from the nearest neighbor distributions derived for random particle distributions (Fig. 6D and E; black: 2-wk data; blue: 4-wk data; red: Monte Carlo simulations for random distributions). Compared with the prediction for a random distribution, observed distributions were narrower, displaying a sharp peak at nearest neighbor distances of 19 nm (2 wk; Fig. 6D) and of 14 nm (4 wk; Fig. 6E). These results suggest that VGCC labels are not distributed randomly in AZs and that they form clusters both at 2 wk and at 4 wk. Finally, distributions of all interparticle distances as well as of nearest neighbor distances revealed a shift to shorter values at 4 wk compared with 2 wk, indicating denser clusters at 4 wk than at 2 wk (Fig. 6C and F).

Next, we quantitatively analyzed the VGCC clusters in individual AZs (Fig. 7). To define a cluster, we set a threshold value of 40 nm for the distance between particles belonging to the same cluster. This value was calculated as equal to  $\mu + 3\sigma$ , where  $\mu$  and  $\sigma$  are the mean (18.7 nm) and SD (7.1 nm) obtained for a single Gaussian fit of a 2-wk nearest neighbor distance distribution; it is very close to the value of 42 nm used previously by Althof et al. (30). Fig. 7A–C and D–F, respectively, show examples of cluster analysis at 2 wk and 4 wk. We obtained a histogram of cluster numbers ( $N_C$ ) ranging from 1 to 8 at 2 wk (Fig. 7G) and from 1 to 5 at 4 wk (Fig. 7H), showing significantly different distributions (Fig. 7I). Average  $N_C$  values are  $2.84 \pm 1.48$  for 2 wk and  $2.37 \pm 1.11$  for 4 wk (mean  $\pm$  SD). The number of clusters correlated with the size of AZ area (Fig. 7J and K). The slope of the regression line was steeper at 4 wk (density: 85.5 clusters/ $\mu\text{m}^2$ ) than at 2 wk (61.0 clusters/ $\mu\text{m}^2$ ). The distance between the centers of the clusters calculated by averaging coordinates of all particles in individual clusters was significantly shorter at 4 wk (Fig. 7L), indicating that clusters are more densely organized at 4 wk. However, the means of nearest neighbor distance between clusters are identical at 2 wk (97.4 nm  $\pm$  32.1 nm, mean  $\pm$  SD) and 4 wk (96.7 nm  $\pm$  24.7 nm (Fig. 7M). This result suggests that the higher cluster density at 4 wk arises from a more compact arrangement of clusters within the AZ, and not from a shorter intercluster distance.

To test the dependence of  $N_C$  values on the  $\mu + 3\sigma$  criterion, we also performed analyses using a  $\mu + 2\sigma$  criterion (giving a cutoff at 32.9 nm, probably too restrictive) as well as a  $\mu + 4\sigma$  criterion (giving a cutoff at 47.1 nm, probably too permissive). These analyses (Fig. S5) indicate that  $N_C$  values remain within 15% of their reference obtained with the  $\mu + 3\sigma$  criterion so that overall the results are little affected by the definition of the threshold distance for clusters.

Returning to the 40-nm cutoff, the number of particles in clusters was  $8.79 \pm 7.10$  at 2 wk and  $9.10 \pm 7.16$  at 4 wk (means  $\pm$  SD; these values are corrected for incomplete  $\text{Ca}_v2.1$ -labeling efficiency). To calculate cluster areas, we drew circles with a radius of 20 nm (half of the threshold value for interparticle distance within a cluster) around gold particles and measured the total area of overlapping circles. The cluster area size was correlated with the number of  $\text{Ca}_v2.1$  particles in clusters with respective means of  $4,820 \text{ nm}^2 \pm 3,500 \text{ nm}^2$  at 2 wk and  $4,330 \text{ nm}^2 \pm 2,820 \text{ nm}^2$  at 4 wk (mean  $\pm$  SD; particle density per cluster, 0.00123/ $\text{nm}^2$  at 2 wk and 0.00149/ $\text{nm}^2$  at 4 wk; Fig. 7N and O). Corresponding cluster diameters are 39 nm at 2 wk and 37 nm at 4 wk, assuming a circular cluster shape. These results indicate that one cluster has roughly the same size as a SV. Overall, these results indicate that, with age, the structure of individual VGCC clusters changes toward a smaller and denser conformation.

Finally, we classified the distributions of VGCC clusters in single AZs as “single” (Fig. 8A), “double” (Fig. 8B), “linear” (Fig. 8C), “peripheral” (Fig. 8D), or “mixed” (Fig. 8E). Comparison of 2-wk and 4-wk data reveals an increase of the proportion of double and peripheral types and a reduction of the mixed type at

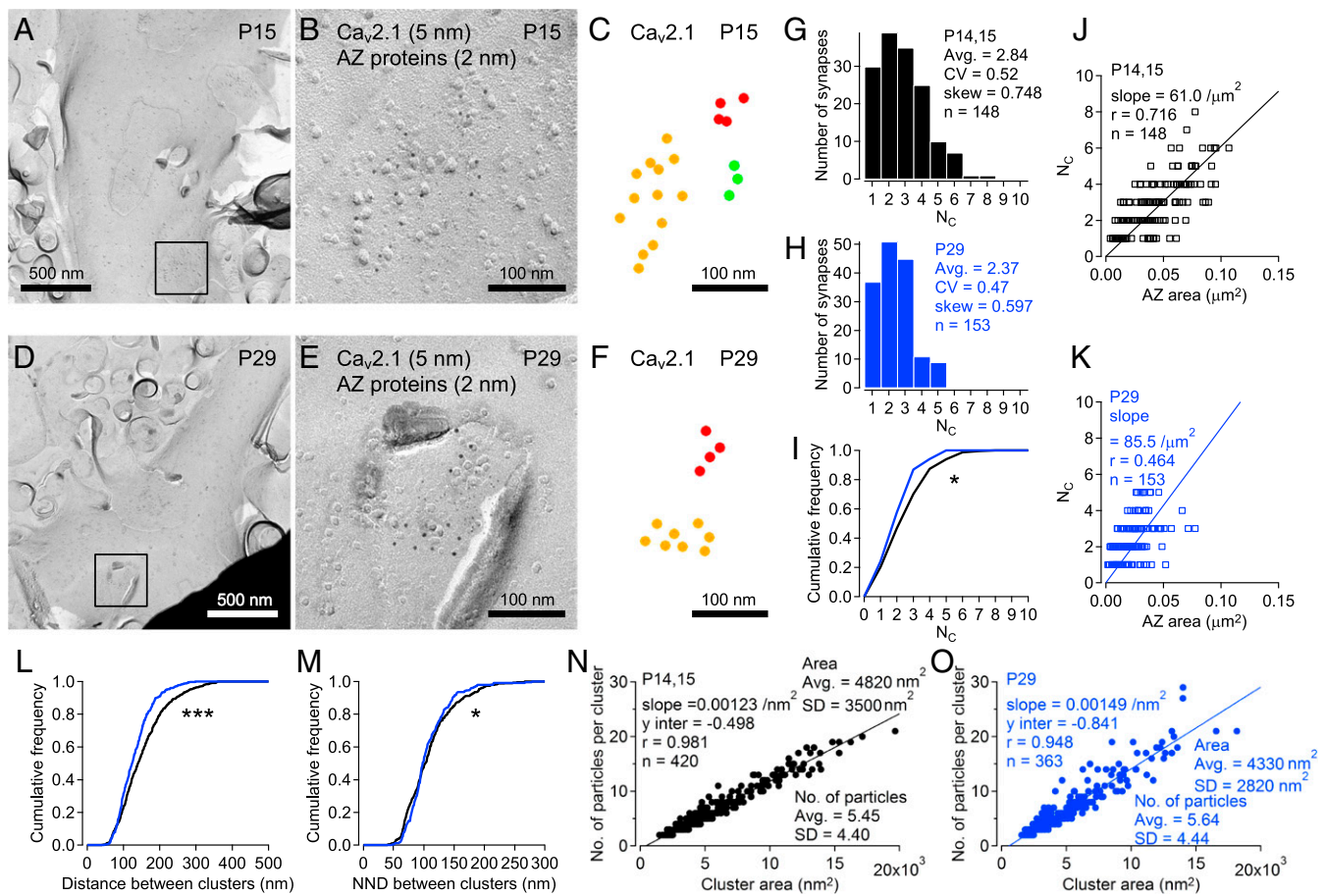


**Fig. 7.** Developmental changes of the distribution of  $Ca_v2.1$  channel clusters in AZs. (A–F) Representative distributions of  $Ca_v2.1$  clusters in individual AZs at 2 wk (A–C) and 4 wk (D–F). (B and E) Extended images of A (B) and D (E). (C and F) Positions of gold particles labeling  $Ca_v2.1$  with color-coded clusters. (G and H) Distribution histograms for the number of  $Ca_v2.1$  clusters per AZ ( $N_C$ ) at 2 wk (G: mean  $\pm$  SD =  $2.84 \pm 1.48$ ) and 4 wk (H: mean  $\pm$  SD =  $2.37 \pm 1.11$ ). (I) Cumulative  $N_C$  distributions at 2 wk and 4 wk. (J and K) Correlation between  $N_C$  and AZ area at 2 wk (J) and 4 wk (K). (L) Cumulative frequency plots for the distance between  $Ca_v2.1$  clusters in AZ at 2 wk (black) and 4 wk (blue). (M) Cumulative frequency plots for nearest neighbor distance between clusters at 2 wk (black) and 4 wk (blue). (N and O) Plots of the number of gold particles in a cluster against cluster area at 2 wk (N:  $n = 420$  clusters) and 4 wk (O:  $n = 363$  clusters). To calculate cluster area, we drew circles with a radius of 20 nm around gold particles labeling  $Ca_v2.1$  and measured the total area of overlapping circles. The average particle numbers per cluster are  $5.45 \pm 4.40$  at 2 wk, and  $5.64 \pm 4.44$  at 4 wk (mean  $\pm$  SD). The average cluster areas are  $4,820 \pm 3,500$  nm<sup>2</sup> at 2 wk and  $4,330 \pm 2,820$  nm<sup>2</sup> at 4 wk. \* $P < 0.05$  and \*\*\* $P < 0.001$ , Kolmogorov–Smirnov test.

4 wk without significant changes in the proportions of the other types (Fig. 8 F and G).

**Correlation Between Docking Sites and  $Ca_v2.1$  Channel Clusters.** Based on the above data it is possible to compare numbers for docking sites ( $N_D$ ) and for  $Ca_v2.1$  channel clusters ( $N_C$ ). After correction for recording bias, mean  $N_D$  values are 3.15 and 2.03 at 2 wk and 4 wk, respectively, whereas mean  $N_C$  values are 2.84 and 2.37 at 2 wk and 4 wk, respectively. Thus, the  $N_D/N_C$  ratio is 1.11 at 2 wk and 0.86 at 4 wk with a mean between these two values of 0.98, which is very close to 1. In addition, the ranges of values are similar for  $N_D$  (1–10 at 2 wk and 1–4 at 4 wk) and for  $N_C$  (1–8 at 2 wk and 1–5 at 4 wk). Finally,  $N_D$  and  $N_C$  change in parallel directions with age, with respective 4-wk and 2-wk ratios of 0.64 and 0.83. Based on these results, we propose that VGCC clusters constitute an essential part of docking sites with a stoichiometry of one docking site per cluster.

It may be asked to what extent this conclusion depends on correcting  $N_D$  values for recording bias. If this correction were omitted, the mean  $N_D/N_C$  ratio would be 1.44, that is, still closer to 1 than to 2. Therefore, the conclusion concerning the docking site is that cluster stoichiometry does not depend on correcting  $N_D$ .

## Discussion

This study suggests that, at PF–MLI synapses, VGCC clusters constitute morphological substrates for functionally defined SV docking sites and that docked SVs associate with VGCC clusters on a one-to-one basis.

**Intersynaptic Variations Are Orchestrated by Synaptic Size.** In addition to numerical comparisons between  $N_D$  and  $N_C$  concerning mean values, ranges, and age-related changes, our results provide indications of possible cellular mechanisms underlying intersynaptic variations of VGCC clusters and SV docking sites. An important clue is that  $N_D$  is correlated with quantal size at simple PF–MLI synapses (Fig. 1H), confirming and extending previous results at simple MLI–MLI synapses (10, 11). This correlation presumably results from a series of intermediate links. It has been suggested that quantal size is linked to the number of postsynaptic receptors, which is itself determined by the PSD area (36, 38). At PF–MLI synapses, the density of AMPA receptors in the PSD is remarkably high (37), so that, despite the small PSD size, the mean quantal size is very large. However, this density remains constant, whereas PSD sizes vary, so that differences in PSD areas translate into differences in receptor numbers (37) and therefore in quantal sizes (9) as shown in this work. Furthermore, it is well

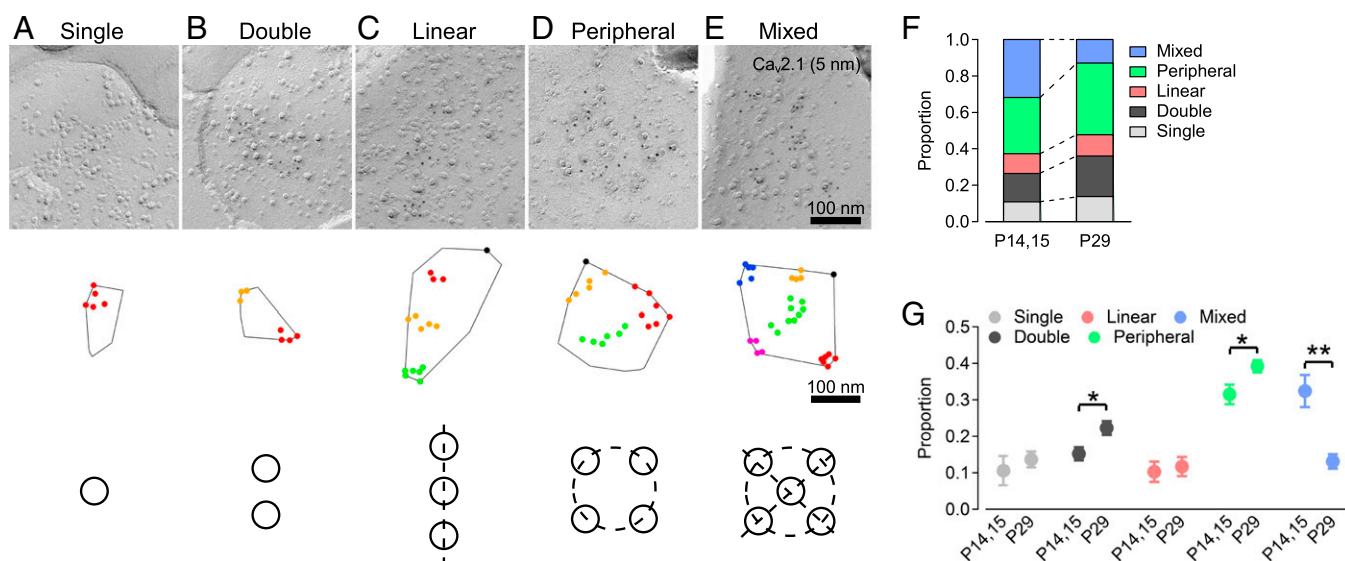


**Fig. 8.** Various categories of  $\text{Ca}_v2.1$  channel cluster distributions. (A–E) Representative images (Upper row), positions of particles (Middle row), and schematics (Lower row) for distinct cluster patterns: single (A), double (B), linear (C), peripheral (D), and mixed (E). Clusters are depicted by uniform particle colors in the Middle row (with AZ border indicated by continuous lines), and by open circles in the Lower row. (F) Relative proportions of various patterns of cluster distribution at 2 wk and 4 wk. (G) Absolute proportions of cluster patterns at 2 wk ( $n = 4$  replica samples from two animals) and at 4 wk ( $n = 4$  replica samples from two animals) showing increasing predominance of peripheral pattern.  $P$  values were obtained by Student's  $t$  test.

established that PSD and AZ areas are tightly matched (e.g., 46), as confirmed in the present work (Fig. S4). Finally, our results indicate that AZ area and  $N_C$  are correlated (Fig. 7J and K), so that docking-site density is roughly constant within the AZ at a given age. This last result is in line with previous electron microscopy data showing a correlation between AZ area and number of docked SVs (26, 28, 46). Altogether, this series of correlations accounts for the link between  $N_C$  and quantal size. Under our assumption that  $N_C$  and  $N_D$  are equal, they also account for the observed link between  $N_D$  and quantal size. When examined as a function of age, all of the above parameters ( $N_D$ , quantal size, PSD area, AZ area, and  $N_C$ ) tend to decrease together due to a general adjustment of the synapse to a smaller size.

**Changes of Synaptic Properties with Age.** Our results reveal complex changes of synaptic properties between 2 wk and 4 wk. First, our findings indicate a developmental sharpening of synaptic organization and function at the level of simple synapses. Morphologically, the sizes of both the AZ and the PSD decrease with age, together with the number of VGCC clusters. A similar reduction during development of the AZ surface area has been previously reported at the calyx of Held (28). Functionally, we find a decreased signaling of simple PF–MLI synapses with age. This fact is due to the combination of three separate effects: a decrease of the quantal size; a decrease of  $N_D$ ; and a decrease in the probability of release at each docking site. Our finding of a decrease in quantal size between 2 wk and 4 wk is consistent with a similar decrease at MLI–MLI synapses (47) but contrasts with the reported increase at the calyx of Held between 1 wk and 2 wk (48). The finding of a decrease of  $N_D$  is consistent with our finding of a decrease in the quantal size, given the correspondence between the sizes of pre- and postsynaptic structures at simple synapses (46). It is also in accord with an earlier report of a decrease with age in the number of docked SVs at calyx AZs (28). Finally, the finding of a decrease in release probability is consistent with previous results at several types of central synapses (47–50; but see 32). In the calyx of Held this decrease is associated with a shortening of the AP waveform (51) and a consequent decrease of  $\text{Ca}^{2+}$  entry (34).

Second, a similar sharpening occurs at the level of VGCCs. Although numbers of VGCCs per cluster are similar at 2 wk and

4 wk, the density of channels within each cluster, like the density of clusters within the AZ, is higher at 4 wk than at 2 wk. This tighter VGCC arrangement presumably allows for more efficient coupling between  $\text{Ca}^{2+}$  entry and SV release at 4 wk compared with 2 wk and is consistent with the finding that the blocking efficiency of EGTA on transmitter release decreases with age at the calyx of Held (34, 52, 53; review: ref. 16), at PF–PC synapses (32), and at amacrine cell synapses (54). Likewise, recent morphological data show an age-dependent tightening of the VGCC–SV arrangement in AZs of the fly neuromuscular junction (23).

Altogether, it appears that at PF–MLI synapses several factors contribute to improving the efficiency of synaptic function during development, both at the level of simple synapses and at the level of single docking sites. These adaptations may be seen as a way to spare metabolic costs in a maturing neuronal circuit.

**Site of SV Fusion.** Recent models developed at the calyx of Held (“exclusion zone model”) (55) (“perimeter release model”) (34) do not incorporate any restriction in the number of SVs released per VGCC cluster. By contrast, functional data at PF–MLI simple synapses imply that at most  $N_C$  SVs are released per docking site and per AP (9, 29; this work) (Fig. S2). Based on the present finding that  $N_D$  and  $N_C$  are equal, we propose that, at PF–MLI synapses, either 0 or 1 fusion-competent SV is docked per VGCC cluster. This model is similar to the proposed association of precisely defined docking sites with a cluster of cacophony channels at the fly neuromuscular junction (23, 24) with the important difference that, in the fly, several docking sites are associated with one VGCC cluster, whereas we propose here a one-to-one stoichiometry.

Our results indicate an intercluster center-to-center distance of 97 nm at both 2 wk and 4 wk, representing twice the SV diameter. Because each cluster itself has a diameter of 37–39 nm, roughly the size of a SV, there is space for only one SV between two clusters. Thus, each VGCC cluster is surrounded by sufficient free space to allow SV fusion in any direction. However, only a fraction of this space is suitable for SV docking because we find that VGCC clusters are often located at the periphery of the AZ (Fig. 8). Future investigations will be required to define the cellular mechanisms responsible for the one-to-one stoichiometry observed between VGCC clusters and docking sites.



Another remaining source of uncertainty concerns SV supply. Docking-site replenishment is a  $\text{Ca}^{2+}$ -driven process (3) that depends on filament-like links between SVs and plasma membrane (20, 24, 56, 57), possibly involving actin and myosin II (58–61). In PF–MLI synapses, recent results indicate that an empty docking site is resupplied by a replacement SV that moves toward the docking site by a cytoskeleton-driven transition (two-step model) (29). Because this movement depends on  $\text{Ca}^{2+}$ , the VGCC cluster associated with the docking site is actually used twice, once for loading the docking site and again for exocytosis. However, it remains unclear how replacement SV and docked SV are positioned in relation with the VGCC cluster.

## Materials and Methods

**General Recording Procedures.** Sagittal slices (200  $\mu\text{m}$  thick) were prepared from the cerebellar vermis of Sprague–Dawley rats (P12–P29) following the animal care guidelines of Université Paris Descartes (approval no. A-750607). Procedures to record from MLI were as described (62). About 2/3 of the recordings were from basket cells, defined as MLIs located in the proximal third of the molecular layer, and the remaining 1/3 were stellate cells. This percentage applies to all electrophysiology data. The composition of the standard extracellular solution was (in mM): 130 NaCl, 2.5 KCl, 26  $\text{NaHCO}_3$ , 1.3  $\text{NaH}_2\text{PO}_4$ , 10 glucose, 2  $\text{CaCl}_2$ , and 1  $\text{MgCl}_2$ ; osmolarity: 300 mosm. This solution was equilibrated with 95%  $\text{O}_2$  and 5%  $\text{CO}_2$  (pH 7.4). The standard internal recording solution contained (in mM): 144 K-glutamate, 6 KCl, 4.6  $\text{MgCl}_2$ , 1 EGTA, 0.1  $\text{CaCl}_2$ , 10 Hepes-K, 4 ATP-Na, 0.4 GTPNa; pH 7.3; osmolarity: 300 mosm. Recordings were at 30–34 °C.

**Simple Synapse Recording.** Extracellular stimulation and recording of simple PF–MLI synapses were obtained under voltage clamp at  $-60$  mV. For extracellular stimulation, a monopolar pipette was filled with internal solution. To record from simple synapses, the extracellular solution was switched to a new solution containing 3 mM external calcium to enhance release probability. NMDA receptors and  $\text{GABA}_A$  receptors were blocked by inclusion of  $\text{D}(-)$ -2-amino-5-phosphonopentanoic acid (50  $\mu\text{M}$ ) and gabazine (15  $\mu\text{M}$ ). To find an appropriate location for electrical stimulation, we puff-applied the internal solution including 150 mM  $\text{K}^+$  from the monopolar pipette using small pressure steps while moving the pipette in the GC layer. When we found a burst-like EPSC response in the postsynaptic cell, we gradually reduced the pressure of puffing to better define the spot for stimulation. Having found postsynaptic responses with minimum puff applications of the high-K solution, we switched to electrical stimulation, keeping the same stimulation pipette, and we further optimized the pipette location to minimize the intensity needed to stimulate the connected GC. At this stage, it was often possible to identify visually the presynaptic GC. Therefore, in one variant procedure (paired recordings), the presynaptic GC was recorded in the cell-attached condition, and corresponding simple synapse EPSCs were obtained by applying large-amplitude voltage steps to the presynaptic GC. Alternatively, extracellular stimulation was applied by using voltage steps of 10–40 V (0.1–0.18 ms of duration). During recording, amplitudes of late events were visually inspected, and if these amplitudes appeared heterogeneous, the corresponding stimulation site was abandoned. Definitive acceptance of the experiment as a usable simple synapse recording occurred after analysis and depended on three criteria (9): (i) a decrement of EPSC amplitudes of second events in a pair, reflecting activation of a common set of receptors belonging to one PSD; (ii) a Gaussian distribution of EPSC amplitudes with a coefficient of variation (CV) less than 0.5; and (iii) stability of the overall responsiveness over time. Trains of eight such stimulation pulses (interstimulus interval: 5 ms) were applied repetitively, with intervals of 10 s between trains. Statistical data were derived from sequences of 10–30 trains.

**SDS-FRL.** SDS-FRL was performed using some modifications (37, 63–65) of the original technique developed by Fujimoto (66). Sagittal slices (thickness: 200  $\mu\text{m}$ ) were prepared from the cerebellar vermis of Sprague–Dawley rats (P14, P15, and P29) in the same way as for electrophysiological experiments, followed by immersion fixation with 2% paraformaldehyde in phosphate buffer (PB; 0.1 M; pH 7.4) for 2 h at room temperature (22–24 °C). Sagittal sections (thickness: 70  $\mu\text{m}$ ) were cut from fixed slices using a vibrating micro-slicer (Linear-Pro7, Dosaka) in PB. The sections were immersed in graded

glycerol of 15–30% in PB at 4 °C overnight and then rapidly frozen by use of a high-pressure freezing machine (HPM010, BAL-TEC, Balzers). Frozen samples were then fractured at  $-140$  °C by a double-replica method in a freeze-etching device (BAF060, BAL-TEC). Fractured faces were replicated by sequential deposition of carbon (thickness: 5 nm from a 90 ° angle, rotating), platinum-carbon (thickness: 2 nm from a 60 ° angle, unidirectional), and carbon again (thickness: 15 nm from a 90 ° angle, rotating). Nonreplicated tissue was solubilized in a solution containing 15 mM Tris-HCl, 20% sucrose, and 2.5% SDS, pH 8.3, with gentle shaking at 77 °C for 9 h (P14, P15) or 18 h (P29), respectively. The replicas were washed three times in Tris-buffered saline (TBS; 50 mM, pH 7.4) containing 0.05% BSA, and nonspecific binding sites were then blocked with 5% BSA in TBS for 1 h at room temperature.

In single-labeling experiments, the primary antibody (anti-rabbit Kv4.3; 3  $\mu\text{g}/\text{mL}$ ; Alomone Laboratories) was applied in TBS containing 2% BSA for 3 d at 15 °C. Rabbit anti-neurexin antibody was generated using nine amino acid residues common to neurexin 1–3 and belonging to the C-terminal region. Specificity of this antibody was verified by Western blot analysis (Fig. S6) using mouse brain homogenate and immunoprecipitate pulled down with GST-CASK-D [pGEXCASK3–25 (328–909)] as described previously (67). For multiple labeling experiments for AZ proteins with VGLUT1 or VGAT, primary antibodies were applied simultaneously: ELKS, 2  $\mu\text{g}/\text{mL}$  (68); RIM1/2, 2  $\mu\text{g}/\text{mL}$  (Synaptic Systems); neurexins, 2  $\mu\text{g}/\text{mL}$ ; VGLUT1, 2  $\mu\text{g}/\text{mL}$  (Frontier Institute); VGAT, 5  $\mu\text{g}/\text{mL}$  (Synaptic Systems). The replicas were then washed in TBS containing 0.05% BSA three times for 10 min each at room temperature and incubated overnight at room temperature with anti-rabbit secondary antibodies conjugated to 2-nm gold particles (British Biocell International) for AZ proteins, anti-guinea pig secondary antibodies conjugated to 10-nm gold particles for VGLUT1, or anti-mouse secondary antibodies conjugated to 15-nm gold particles for VGAT. In the case of multiple labeling experiments for  $\text{Ca}_v2.1$  with AZ proteins (ELKS, RIM, and neurexin), replicas were first incubated with the  $\text{Ca}_v2.1$  antibody (8  $\mu\text{g}/\text{mL}$ , Frontier Institute) (69) for 3 d at 15 °C and then with anti-guinea pig secondary antibodies conjugated to 5-nm gold particles overnight at 15 °C followed by incubation with the AZ protein antibodies (2  $\mu\text{g}/\text{mL}$  for ELKS, RIM, and neurexin) for 2 d at 15 °C, and finally with anti-rabbit secondary antibodies conjugated to 2-nm gold particles for AZ proteins overnight at 15 °C. After immunogold labeling, the replicas were rinsed three times with 0.05% BSA/TBS, washed with TBS and distilled water, and mounted on formvar-coated 100-line copper grids.

For measurement of intramembrane particle cluster area and quantification of  $\text{Ca}_v2.1$  immunolabeling density, labeled replicas were examined in a Tecnai-12 transmission electron microscope (FEI; AV 120 kV). Image acquisition used magnifications of 97 kx and 135 kx. The  $\text{Ca}_v2.1$  antibody used in this study revealed labeling only at the P-face of the plasma membrane, whereas no labeling was found at the E-face. Immunolabeling specificity of the  $\text{Ca}_v2.1$  antibody was confirmed by applying it to cerebellar tissue samples from  $\text{Ca}_v2.1$  KO mice (70). For the measurement of immunogold particle densities, profiles of presynaptic AZs were tilted in the electron beam to attain a planar view. Data from two animals (two samples from each animal) were pooled together because neither the Kruskal–Wallis's test nor the Mann–Whitney  $U$  test showed significant differences.

**Criteria for AZ Boundaries.** Two steps were undertaken for restricting measurements of AZ areas to single AZs. To avoid sampling of particles outside the synaptic area, we first eliminated images where the longest distance between 2/5 nm gold particles in the defined AZ region was  $>450$  nm for 2 wk and  $>320$  nm for 4 wk, corresponding to the respective maximum sizes observed for the PSD area. To exclude segregated synapses (Fig. S7), we eliminated cases where a single gold particle or the center of an individual particle cluster was  $>150$  nm away from the nearest particle cluster. The threshold of 150 nm was derived from the shortest distance observed between IMP clusters on the E-face of MLI dendrites.

**ACKNOWLEDGMENTS.** We thank Isabel Llano and Erwin Neher for comments on the manuscript and Akari Hagiwara and Toshihisa Ohtsuka for anti-ELKS antibody. This work was supported by a European Research Council Advanced Grant (“SingleSite”) to A.M. and benefited from the Japan Society for the Promotion of Science Core-to-Core Program A (Advanced Research Networks).

1. Südhof TC (2012) The presynaptic active zone. *Neuron* 75:11–25.
2. Clements JD (2003) Variance-mean analysis: A simple and reliable approach for investigating synaptic transmission and modulation. *J Neurosci Methods* 130:115–125.

3. Neher E, Sakaba T (2008) Multiple roles of calcium ions in the regulation of neurotransmitter release. *Neuron* 59:861–872.
4. Kavalali ET, Jorgensen EM (2014) Visualizing presynaptic function. *Nat Neurosci* 17:10–16.

5. Midorikawa M, Sakaba T (2015) Imaging exocytosis of single synaptic vesicles at a fast CNS presynaptic terminal. *Neuron* 88:492–498.
6. Tang A-H, et al. (2016) A trans-synaptic nanocolumn aligns neurotransmitter release to receptors. *Nature* 536:210–214.
7. Takahashi T (2015) Strength and precision of neurotransmission at mammalian presynaptic terminals. *Proc Jpn Acad, Ser B, Phys Biol Sci* 91:305–320.
8. Ritzau-Jost A, et al. (2014) Ultrafast action potentials mediate kilohertz signaling at a central synapse. *Neuron* 84:152–163.
9. Malagon G, Miki T, Llano I, Neher E, Marty A (2016) Counting vesicular release events reveals binomial release statistics at single glutamatergic synapses. *J Neurosci* 36:4010–4025.
10. Pulido C, Trigo FF, Llano I, Marty A (2015) Vesicular release statistics and unitary postsynaptic current at single GABAergic synapses. *Neuron* 85:159–172.
11. Trigo FF, Sakaba T, Ogden D, Marty A (2012) Readily releasable pool of synaptic vesicles measured at single synaptic contacts. *Proc Natl Acad Sci USA* 109:18138–18143.
12. Imig C, et al. (2014) The morphological and molecular nature of synaptic vesicle priming at presynaptic active zones. *Neuron* 84:416–431.
13. Llinás R, Steinberg IZ, Walton K (1981) Relationship between presynaptic calcium current and postsynaptic potential in squid giant synapse. *Biophys J* 33:323–351.
14. Eggermann E, Bucurenciu I, Goswami SP, Jonas P (2011) Nanodomain coupling between  $\text{Ca}^{2+}$  channels and sensors of exocytosis at fast mammalian synapses. *Nat Rev Neurosci* 13:7–21.
15. Stanley EF (2016) The nanophysiology of fast transmitter release. *Trends Neurosci* 39:183–197.
16. Wang LY, Augustine GJ (2015) Presynaptic nanodomains: A tale of two synapses. *Front Cell Neurosci* 8:455.
17. Couteaux R, Pécot-Dechavassine M (1970) Synaptic vesicles and pouches at the level of 'active zones' of the neuromuscular junction. *C R Hebd Séances Acad Sci D* 271:2346–2349.
18. Heuser JE, et al. (1979) Synaptic vesicle exocytosis captured by quick freezing and correlated with quantal transmitter release. *J Cell Biol* 81:275–300.
19. Harlow ML, Ress D, Stoschek A, Marshall RM, McMahan UJ (2001) The architecture of active zone material at the frog's neuromuscular junction. *Nature* 409:479–484.
20. Szule JA, et al. (2012) Regulation of synaptic vesicle docking by different classes of macromolecules in active zone material. *PLoS One* 7:e33333.
21. Nagwaney S, et al. (2009) Macromolecular connections of active zone material to docked synaptic vesicles and presynaptic membrane at neuromuscular junctions of mouse. *J Comp Neurol* 513:457–468.
22. Ruiz R, et al. (2011) Active zones and the readily releasable pool of synaptic vesicles at the neuromuscular junction of the mouse. *J Neurosci* 31:2000–2008.
23. Böhm MA, et al. (2016) Active zone scaffolds differentially accumulate Unc13 isoforms to tune  $\text{Ca}^{2+}$  channel-vesicle coupling. *Nat Neurosci* 19:1311–1320.
24. Matkovic T, et al. (2013) The Bruchpilot cytomatrix determines the size of the readily releasable pool of synaptic vesicles. *J Cell Biol* 202:667–683.
25. Xu-Friedman MA, Harris KM, Regehr WG (2001) Three-dimensional comparison of ultrastructural characteristics at depressing and facilitating synapses onto cerebellar Purkinje cells. *J Neurosci* 21:6666–6672.
26. Han Y, Kaeser PS, Südhof TC, Schneggenburger R (2011) RIM determines  $\text{Ca}^{2+}$  channel density and vesicle docking at the presynaptic active zone. *Neuron* 69:304–316.
27. Sätzler K, et al. (2002) Three-dimensional reconstruction of a calyx of Held and its postsynaptic principal neuron in the medial nucleus of the trapezoid body. *J Neurosci* 22:10567–10579.
28. Taschenberger H, Leão RM, Rowland KC, Spirou GA, von Gersdorff H (2002) Optimizing synaptic architecture and efficiency for high-frequency transmission. *Neuron* 36:1127–1143.
29. Miki T, et al. (2016) Actin- and myosin-dependent vesicle loading of presynaptic docking sites prior to exocytosis. *Neuron* 91:808–823.
30. Althoff D, et al. (2015) Inhibitory and excitatory axon terminals share a common nanoarchitecture of their  $\text{Ca}_v2.1$  (P/Q-type)  $\text{Ca}^{2+}$  channels. *Front Cell Neurosci* 9:315.
31. Holderith N, et al. (2012) Release probability of hippocampal glutamatergic terminals scales with the size of the active zone. *Nat Neurosci* 15:988–997.
32. Baur D, et al. (2015) Developmental tightening of cerebellar cortical synaptic influx-release coupling. *J Neurosci* 35:1858–1871.
33. Indriati DW, et al. (2013) Quantitative localization of  $\text{Ca}_v2.1$  (P/Q-type) voltage-dependent calcium channels in Purkinje cells: Somatodendritic gradient and distinct somatic coclustering with calcium-activated potassium channels. *J Neurosci* 33:3668–3678.
34. Nakamura Y, et al. (2015) Nanoscale distribution of presynaptic  $\text{Ca}^{2+}$  channels and its impact on vesicular release during development. *Neuron* 85:145–158.
35. Ishiyama S, Schmidt H, Cooper BH, Brose N, Eilers J (2014) Munc13-3 superprimers synaptic vesicles at granule cell-to-basket cell synapses in the mouse cerebellum. *J Neurosci* 34:14687–14696.
36. Auger C, Marty A (1997) Heterogeneity of functional synaptic parameters among single release sites. *Neuron* 19:139–150.
37. Masugi-Tokita M, et al. (2007) Number and density of AMPA receptors in individual synapses in the rat cerebellum as revealed by SDS-digested freeze-fracture replica labeling. *J Neurosci* 27:2135–2144.
38. Nusser Z, Cull-Candy S, Farrant M (1997) Differences in synaptic GABA<sub>A</sub> receptor number underlie variation in GABA mini amplitude. *Neuron* 19:697–709.
39. Lee JS, Ho W-K, Neher E, Lee S-H (2013) Superpriming of synaptic vesicles after their recruitment to the readily releasable pool. *Proc Natl Acad Sci USA* 110:15079–15084.
40. Taschenberger H, Woehler A, Neher E (2016) Superpriming of synaptic vesicles as a common basis for intersynapse variability and modulation of synaptic strength. *Proc Natl Acad Sci USA* 113:E4548–E4557.
41. Mintz IM, Sabatini BL, Regehr WG (1995) Calcium control of transmitter release at a cerebellar synapse. *Neuron* 15:675–688.
42. Hsu Y-H, Huang H-Y, Tsaur M-L (2003) Contrasting expression of Kv4.3, an A-type K<sup>+</sup> channel, in migrating Purkinje cells and other post-migratory cerebellar neurons. *Eur J Neurosci* 18:601–612.
43. Miyazaki T, Fukaya M, Shimizu H, Watanabe M (2003) Subtype switching of vesicular glutamate transporters at parallel fibre-Purkinje cell synapses in developing mouse cerebellum. *Eur J Neurosci* 17:2563–2572.
44. Harris KM, Landis DMD (1986) Membrane structure at synaptic junctions in area CA1 of the rat hippocampus. *Neuroscience* 19:857–872.
45. Landis DMD, Reese TS (1974) Differences in membrane structure between excitatory and inhibitory synapses in the cerebellar cortex. *J Comp Neurol* 155:93–125.
46. Schikorski T, Stevens CF (1997) Quantitative ultrastructural analysis of hippocampal excitatory synapses. *J Neurosci* 17:5858–5867.
47. Pouzat C, Hestrin S (1997) Developmental regulation of basket/stellate cell→Purkinje cell synapses in the cerebellum. *J Neurosci* 17:9104–9112.
48. Taschenberger H, Scheuss V, Neher E (2005) Release kinetics, quantal parameters and their modulation during short-term depression at a developing synapse in the rat CNS. *J Physiol* 568:513–537.
49. Frick A, Feldmeyer D, Sakmann B (2007) Postnatal development of synaptic transmission in local networks of L5A pyramidal neurons in rat somatosensory cortex. *J Physiol* 585:103–116.
50. Reyes A, Sakmann B (1999) Developmental switch in the short-term modification of unitary EPSPs evoked in layer 2/3 and layer 5 pyramidal neurons of rat neocortex. *J Neurosci* 19:3827–3835.
51. Taschenberger H, von Gersdorff H (2000) Fine-tuning an auditory synapse for speed and fidelity: Developmental changes in presynaptic waveform, EPSC kinetics, and synaptic plasticity. *J Neurosci* 20:9162–9173.
52. Fedchyshyn MJ, Wang L-Y (2005) Developmental transformation of the release modality at the calyx of Held synapse. *J Neurosci* 25:4131–4140.
53. Wang L-Y, Neher E, Taschenberger H (2008) Synaptic vesicles in mature calyx of Held synapses sense higher nanodomain calcium concentrations during action potential-evoked glutamate release. *J Neurosci* 28:14450–14458.
54. Balakrishnan V, Puthusseri T, Kim M-H, Taylor WR, von Gersdorff H (2015) Synaptic vesicle exocytosis at the dendritic lobules of an inhibitory interneuron in the mammalian retina. *Neuron* 87:563–575.
55. Keller D, et al. (2015) An exclusion zone for  $\text{Ca}^{2+}$  channels around docked vesicles explains release control by multiple channels at a CNS synapse. *PLOS Comput Biol* 11:e1004253.
56. Cole AA, Chen X, Reese TS (2016) A network of three types of filaments organizes synaptic vesicles for storage, mobilization, and docking. *J Neurosci* 36:3222–3230.
57. Siksou L, et al. (2007) Three-dimensional architecture of presynaptic terminal cytomatrix. *J Neurosci* 27:6868–6877.
58. Lee JS, Ho W-K, Lee S-H (2012) Actin-dependent rapid recruitment of reluctant synaptic vesicles into a fast-releasing vesicle pool. *Proc Natl Acad Sci USA* 109:E765–E774.
59. Peng A, Rotman Z, Deng P-Y, Klyachko VA (2012) Differential motion dynamics of synaptic vesicles undergoing spontaneous and activity-evoked endocytosis. *Neuron* 73:1108–1115.
60. Hallermann S, Silver RA (2013) Sustaining rapid vesicular release at active zones: Potential roles for vesicle tethering. *Trends Neurosci* 36:185–194.
61. Körber C, Künér T (2016) Molecular machines regulating the release probability of synaptic vesicles to the active zone. *Front Synaptic Neurosci* 8:5.
62. Llano I, Gerschenfeld HM (1993) Inhibitory synaptic currents in stellate cells of rat cerebellar slices. *J Physiol* 468:177–200.
63. Kasugai Y, et al. (2010) Quantitative localisation of synaptic and extrasynaptic GABAA receptor subunits on hippocampal pyramidal cells by freeze-fracture replica immunolabelling. *Eur J Neurosci* 32:1868–1888.
64. Masugi-Tokita M, Shigemoto R (2007) High-resolution quantitative visualization of glutamate and GABA receptors at central synapses. *Curr Opin Neurobiol* 17:387–393.
65. Tarusawa E, et al. (2009) Input-specific intrasynaptic arrangements of ionotropic glutamate receptors and their impact on postsynaptic responses. *J Neurosci* 29:12896–12908.
66. Fujimoto K (1995) Freeze-fracture replica electron microscopy combined with SDS digestion for cytochemical labeling of integral membrane proteins. Application to the immunogold labeling of intercellular junctional complexes. *J Cell Sci* 108:3443–3449.
67. Butz S, Okamoto M, Südhof TC (1998) A tripartite protein complex with the potential to couple synaptic vesicle exocytosis to cell adhesion in brain. *Cell* 94:773–782.
68. Deguchi-Tawarada M, et al. (2004) CAST2: Identification and characterization of a protein structurally related to the presynaptic cytomatrix protein CAST. *Genes Cells* 9:15–23.
69. Miyazaki T, et al. (2012)  $\text{Ca}_v2.1$  in cerebellar Purkinje cells regulates competitive excitatory synaptic wiring, cell survival, and cerebellar biochemical compartmentalization. *J Neurosci* 32:1311–1328.
70. Jun K, et al. (1999) Ablation of P/Q-type  $\text{Ca}^{2+}$  channel currents, altered synaptic transmission, and progressive ataxia in mice lacking the  $\alpha_{1A}$ -subunit. *Proc Natl Acad Sci USA* 96:15245–15250.
71. Brenowitz SD, Regehr WG (2007) Reliability and heterogeneity of calcium signaling at single presynaptic boutons of cerebellar granule cells. *J Neurosci* 27:7888–7898.
72. Bischofberger J, Geiger JR, Jonas P (2002) Timing and efficacy of  $\text{Ca}^{2+}$  channel activation in hippocampal mossy fiber boutons. *J Neurosci* 22:10593–10602.
73. Li L, Bischofberger J, Jonas P (2007) Differential gating and recruitment of P/Q-, N-, and R-type  $\text{Ca}^{2+}$  channels in hippocampal mossy fiber boutons. *J Neurosci* 27:13420–13429.